Research Square

Preprints are preliminary reports that have not undergone peer review.
They should not be considered conclusive, used to inform clinical practice,
or referenced by the media as validated information.

Host Dependent Effects of Yttrium Substitution on the Structure Magnetism and Dielectric Response of Spinel Ferrites and Related Magnetic Oxides

R. Sagayaraj

sagayaraj@sjctnc.edu.in

St. Joseph's College of Arts and Science (Autonomous)

K. Veeramuthu

Thiru. Kolanjiappar Government Arts College

R. Nithya

Sree Dattha Institute of Engineering and Science

A. Amalorpavadoss

St. Joseph's College of Arts and Science (Autonomous)

K. B. Bhaskar

Adhi College of Engineering and Technology

Systematic Review

Keywords: Yttrium substitution, Spinel ferrites, Secondary YFeO3 phase, Magnetic properties, Dielectric loss, Microwave absorption, Functional oxides

Posted Date: November 25th, 2026

DOI: https://doi.org/10.21203/rs.3.rs-11600648/v1

License: This work is licensed under a Creative Commons Attribution 4.0 International License.
Read Full License

Additional Declarations: No competing interests reported.

Host Dependent Effects of Yttrium Substitution on the Structure Magnetism and Dielectric Response of Spinel Ferrites and Related Magnetic Oxides

R. Sagayaraj [a,*], K. Veeramuthu [b], R. Nithya [c], A. Amalorpavadoss [d], K. B. Bhaskar [e]

[a]PG & Research Department of Physics, St. Joseph's College of Arts and Science (Autonomous), Cuddalore-607001, Affiliated to Annamalai University, Tamil Nadu, India

[b]PG & Research Department of Physics, Thiru. Kolanjiappar Government Arts College, Virudhachalam-606 001, Affiliated to Annamalai University, Tamil Nadu, India

[c]Department of Physics, Sree Dattha Institute of Engineering and Science, Sheriguda, Telangana- 501510, Affiliated to Jawaharlal Nehru Technological University Hyderabad, India

[d]PG & Research Department of Chemistry, St. Joseph's College of Arts and Science (Autonomous), Cuddalore-607001, Affiliated to Annamalai University, Tamil Nadu, India

[e]Department of Electrical and Electronics Engineering, Adhi College of Engineering and Technology, Kanchipuram, Tamil Nadu, India

Abstract

Yttrium (Y^{3+}) is widely used to tailor spinel ferrites, garnets and perovskite-type magnetic oxides, but its effects are often presented as uniform when they are in fact strongly host-, route- and composition-dependent. Because Y^{3+} (0.90 Å) is much larger than Fe^{3+} (0.645 Å) and has a closed-shell, diamagnetic configuration, its substitution generally expands the lattice, introduces strain, weakens A–B superexchange and lowers saturation magnetization, although exceptions exist. Coercivity can fall or rise depending on the host, and the solubility limit before secondary $YFeO_3$ appears ranges from $x \approx 0.025$ to about 20 mol%, depending on the host, sintering route and iron compensation. Y^{3+} frequently raises resistivity and lowers permittivity and dielectric loss, which is attractive for high-frequency devices. We link these structure–property relations to synthesis routes (sol-gel auto-combustion, co-precipitation, hydrothermal, electrospinning, microwave sintering), to the diagnostic value of XRD, FTIR and Raman data, and to applications in microwave absorption, photocatalysis, gas sensing, electrocatalytic hydrogen evolution and thermochemical CO_2 splitting. Eight tables and nine figures compile verified host-by-host data (including re-plotted literature data and open-access figures), and open challenges are outlined, including iron-compensated stoichiometry, site-occupancy determination, standardized dielectric reporting, benchmarking of thermochemical redox data and device-level integration.

Keywords: Yttrium substitution; Spinel ferrites; Secondary $YFeO_3$ phase; Magnetic properties; Dielectric loss; Microwave absorption; Functional oxides

[*]**Corresponding author:**

R. Sagayaraj (sagayaraj@sjctnc.edu.in)

1. Introduction

Cubic spinel ferrites (MFe_2O_4, M = Co, Ni, Mg, Zn, Cu) [1–3], perovskite ferrites such as $LaFeO_3$ [4] and garnets such as $Y_3Fe_5O_{12}$ [5, 6] remain central to magneto-dielectric technology because of their chemical stability, tunable band gaps and rich magnetic behavior. The distribution of cations over tetrahedral (A) and octahedral (B) sites controls the Fe^{3+}_A–O^{2-}–Fe^{3+}_B superexchange that underlies ferrimagnetism in spinels [3, 7]. Magnetic oxide nanoparticles are used in biomedicine [8–10], and spinel ferrites in particular have been reviewed for medical use and toxicity [11, 12]. Other reported uses include magnetic hyperthermia [13], Fenton-type and photocatalytic water treatment [14–16], microwave absorption [17, 18], supercapacitor electrodes [19–21] and catalysis for hydrogen storage [22]. Pristine compositions nevertheless suffer from limitations such as dielectric loss at high frequency [2, 7] and, in photocatalysis, wide band gaps and fast carrier recombination [4, 23]. Substituting cations in the spinel lattice is the standard remedy. Divalent or trivalent dopants such as Zn, Cd, Mn, Co, Mg and Al have been used to tune structure, magnetism and dielectric behavior of Co, Ni and Mg ferrites [24–33], embedding in a silica matrix has been used for Cu–Co ferrite [34], and rare-earth (RE) ions are a further option. Heavier lanthanides such as Sm^{3+} and Dy^{3+} carry 4f electrons and act through 3d–4f coupling and strong spin–orbit effects [35, 36]. Yttrium behaves differently. Although it is formally a 4d transition metal, its chemistry closely resembles that of the heavy lanthanides and it is conventionally grouped with the rare earths. Its trivalent ion has a closed-shell [Kr] configuration, so it is diamagnetic and has no 4f electrons. Its ionic radius (0.90 Å) is considerably larger than that of Fe^{3+} (0.645 Å; Table 1). Y^{3+} has been introduced into $MnFe_2O_4$ [7, 37], Mn–Zn ferrite together with Dy^{3+} [38], $CoFe_2O_4$ [39–44], $CdFe_2O_4$ [45], $NiFe_2O_4$ [46, 47], Mg–Zn ferrite [3, 48, 49] and $MgFe_2O_4$ [50], and lanthanide doping of Mg ferrite has been explored for Fenton-like catalysis [51]. When Y^{3+} enters a spinel lattice it is generally expected to occupy octahedral sites, expand the cell, strain the lattice and dilute the magnetic sublattice without adding moment of its own [3, 48]. The literature shows, however, that the consequences are not uniform: saturation magnetization usually falls but has been seen to rise [52], coercivity decreases in some hosts and increases in others [3, 50], and the amount of Y^{3+} accepted before orthoferrite ($YFeO_3$) precipitates varies widely [49, 50, 53]. This review therefore organizes the literature around host- and route-dependence. We cover synthesis (Section 2), structural diagnostics (Section 3),

magnetic and dielectric tuning (Section 4), applications including thermochemical fuel production and garnet and perovskite hosts (Section 5), and open problems (Section 6).

2. Synthesis Strategies and Morphological Control

The large Y^{3+} ion strains compact interstitial sites, so the synthesis route and thermal history largely decide how much dopant is incorporated and what secondary phases form (Table 1).

2.1. Sol-gel and auto-combustion routes

In sol-gel auto-combustion (Fig. 1), metal nitrates are chelated with a fuel such as citric acid or sucrose, gelled by heating, and ignited. The self-sustained redox reaction yields a fine, chemically homogeneous ash that is calcined to remove organics and complete crystallization [54, 55]. The route is used for Y-substituted Mg–Zn ferrites with sucrose as fuel [3], Y-doped $MgFe_2O_4$ [50], $CuFe_{2-x}Y_xO_4$ [56], Y-doped $CoFe_2O_4$ [44] and Y/Ce co-doped $NiFe_2O_4$ [57]. Related sol-gel routes include a PVA-based synthesis of $MgFe_2O_4$ [58], sol-gel preparation followed by heat treatment to tune the structural, magnetic and dielectric properties of $MgFe_2O_4$ [59], and citrate-derived Zn-doped $MgFe_2O_4$ [21]. Annealing temperature likewise affects phase and magnetic properties in Ni-substituted yttrium iron garnet [60] and the properties of Al-substituted Ni–Zn ferrite [61]. Rapid laser-furnace processing has been demonstrated for $NiFe_2O_4$ [62], and co-precipitation for Ni-substituted $MgFe_2O_4$ [63]. Because the fuel, heating profile and calcination temperature all influence cation incorporation, nominally identical compositions prepared by different groups can differ in phase purity.

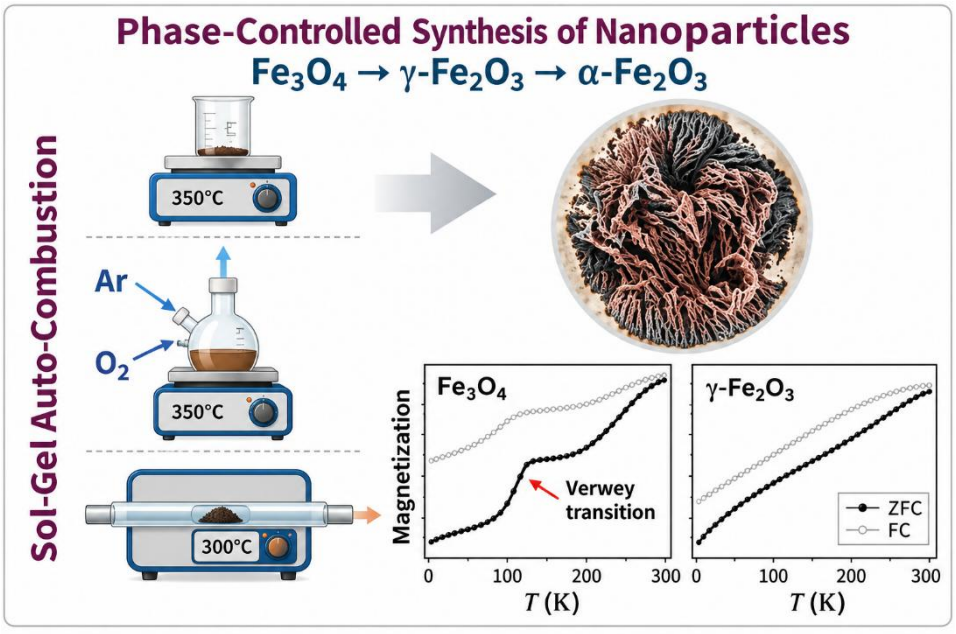

Fig. 1 Schematic of the sol-gel auto-combustion route used for Y^{3+}-substituted spinel ferrites [64]

Charge compensation is a critical and often overlooked variable. In sol-gel Y-doped $MgFe_2O_4$, samples prepared at fixed iron content contained $YFeO_3$ impurity, whereas single-phase compounds were obtained only at 20 mol% Y^{3+} when the iron content was reduced to balance the extra positive charge [50]. Reporting the stoichiometry used for compensation is therefore as important as reporting the nominal Y content.

2.2. Solid-state, co-precipitation and hydrothermal routes

Conventional ceramic processing of $Mg_{0.5}Zn_{0.5}Y_xFe_{2-x}O_4$ ($0 \le x \le 0.05$) gave a single cubic spinel phase up to $x = 0.03$ and $YFeO_3$ at higher Y content [48, 49]. Co-precipitation has been applied to Y-substituted $NiFe_2O_4$ ($x = 0.05, 0.15, 0.3$) [46], to Y-substituted cadmium ferrite [45], and in a combined experimental and computational study of Y-doped nickel ferrite [47]. Hydrothermal synthesis was used for $Co_{0.5}Ni_{0.5}Y_xFe_{2-x}O_4$ over the very wide range $0 \le x \le 1.0$, with attention to X-band microwave absorption [65]. Y-doped $CoFe_2O_4$ prepared by various routes has been examined for catalytic performance [39], structure and electrical behavior [41], and optical and photocatalytic response [43]. Table 1 collects representative routes, hosts and outcomes.

Table 1. Representative synthesis routes for Y-substituted magnetic oxides and reported outcomes.

Route	Host / Y range	Reported outcome	Ref.
Sol-gel combustion (sucrose fuel)	$Mg_{0.6}Zn_{0.4}Y_xFe_{2-x}O_4$, $0 \le x \le 0.3$	Lattice parameter increases (Y^{3+} larger than Mg^{2+}, Zn^{2+}); agglomerated grains; coercivity increases	[3]
Sol-gel (citric acid / ethylene glycol; two iron-content series)	Y-doped $MgFe_2O_4$, up to 20 mol% Y	Fixed Fe: $YFeO_3$ impurity. Single phase only at 20 mol% Y with reduced Fe; Ms and Hc decrease	[50]
Sol-gel auto-combustion + microwave (MST) or conventional (CST) sintering	$Ni_{0.6}Zn_{0.3}Co_{0.1}Y_xFe_{2-x}O_4$, $0 \le x \le 0.1$	$YFeO_3$ forms for $x > 0.025$ in both MST and CST samples; MST samples show better electromagnetic performance	[53]
Solid-state ceramic	$Mg_{0.5}Zn_{0.5}Y_xFe_{2-x}O_4$, $0 \le x \le 0.05$	Single phase to $x = 0.03$, $YFeO_3$ beyond; Curie temperature decreases	[48, 49]
Solid-state reaction	$Ni_{0.5}Co_{0.5}Fe_{2-x}Y_xO_4$, $x \le 0.02$	Magnetization increases from ~55 to ~61 emu/g	[52]
Co-precipitation	$NiFe_{2-x}Y_xO_4$, $x = 0.05, 0.15, 0.3$	Impedance and dielectric dispersion analysed with a constant phase element; largest change at $x = 0.05$	[46]
Co-precipitation	Y-substituted $CdFe_2O_4$	Structural, electrical, optical and dielectric properties studied	[45]
Sol-gel	$BaY_yFe_{2-y}O_4$, $0 \le y \le 0.10$	Cubic structure; $YFeO_3$ forms beyond $y = 0.06$; lattice parameter and resistivity increase	[66]
Hydrothermal	$Co_{0.5}Ni_{0.5}Y_xFe_{2-x}O_4$, $0 \le x \le 1.0$	Structural, magnetic, dielectric and X-band absorption properties studied	[65]
Sol-gel auto-combustion	$CuFe_{2-x}Y_xO_4$, $x = 0.1–0.5$	Stable tetragonal copper ferrite retained with and without doping	[56]
Solution combustion	$NiFe_{2-(x+y)}Y_xCe_yO_4$, $x = y \le 0.02$	Improved HER activity in 1 M KOH	[57]

Electrospinning	Y-doped $NiFe_2O_4$ nanofibers	Enhanced gas-sensing performance with rapid response	[67]
Electrospinning	Y-doped $ZnFe_2O_4$ nanofibers	Gas sensor for n-butanol	[68]

2.3. Sintering: microwave versus conventional

In $Ni_{0.6}Zn_{0.3}Co_{0.1}Y_xFe_{2-x}O_4$ ferrites prepared by sol-gel auto-combustion, microwave sintering gave better structure and electromagnetic performance than conventional sintering at the same Y content. Importantly, a $YFeO_3$ second phase appeared for $x > 0.025$ in both the microwave- and conventionally sintered samples [53], so the solubility limit in that system is set by the host composition rather than by the heating method.

2.4. Low-dimensional morphologies

Beyond nanoparticles, electrospinning produced Y-doped $NiFe_2O_4$ nanofibers [67] and Y-doped $ZnFe_2O_4$ nanofibers [68] for gas sensing. Y/Sn co-doped $BiFeO_3$ has been obtained as 2D nanoplates for dye photodegradation [69], and $Y_{0.045}Ni_{0.045}Fe_{2.91}O_4$ nanowires were decorated over mesoporous silica for crystal violet removal [70]. Such architectures expose more surface area, which is relevant for the surface-controlled applications of Section 5, but the benefit has to be demonstrated against appropriate undoped controls in each case.

3. Structural Modulation and Analytical Techniques

Y^{3+} cannot be imaged directly within the lattice, so its incorporation is inferred from diffraction and vibrational spectroscopy, ideally supported by Rietveld refinement and Mössbauer spectroscopy [50].

3.1. X-ray diffraction and the solubility limit

A frequent finding is expansion of the cubic cell with increasing Y^{3+} content, attributed to the large ionic radius of Y^{3+} relative to the cations it replaces [3, 7]. The expansion is, however, bounded by phase formation. In $Mg_{0.5}Zn_{0.5}Y_xFe_{2-x}O_4$ the experimental lattice constant rose from 8.4309 Å ($x = 0$) to 8.4366 Å ($x = 0.02$) and then fell once $YFeO_3$ appeared at the grain boundaries (8.4288 Å at $x = 0.05$) [48] (Fig. 4a). In Y-doped $MgFe_2O_4$ the diffraction peaks shifted only slightly to lower angle, while the crystallite size dropped from about 40 nm to 10–13 nm [50]. XRD is also the main tool for detecting secondary $YFeO_3$. The composition at which it appears varies widely (Fig. 2, Table 2): $x > 0.025$ in Ni–Zn–Co ferrite [53], $x > 0.03$ in solid-state Mg–Zn ferrite [48, 49], $x \geq 0.15$ in an earlier study of co-precipitated $NiFe_{2-x}Y_xO_4$, as summarized in [46], $y > 0.06$ in sol-gel $BaY_yFe_{2-y}O_4$ [66], and 20 mol% for iron-compensated Mg ferrite, whereas the series without iron compensation was impure at every Y

content [50]. In $CuFe_{2-x}Y_xO_4$, XRD showed the tetragonal structure of copper ferrite persisting on doping [56], a reminder that the host symmetry itself can differ from cubic. The practical conclusion is that a single "solubility limit" for yttrium does not exist; it depends on the host, the cation and oxygen stoichiometry, and the processing route, and the values in Fig. 2 are defined per formula unit on different sites and are not directly comparable.

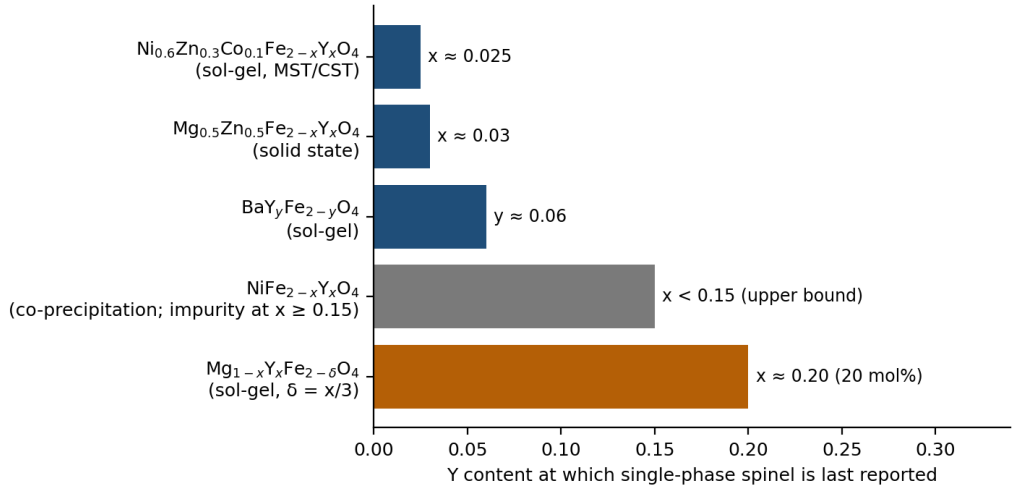

Fig. 2 Reported Y content at which single-phase spinel is last observed in different hosts. Values compiled from [46, 48, 50, 53, 66]; the Ni ferrite bar is an upper bound inferred from the report of a secondary phase at $x \geq 0.15$. Original plot prepared by the authors.

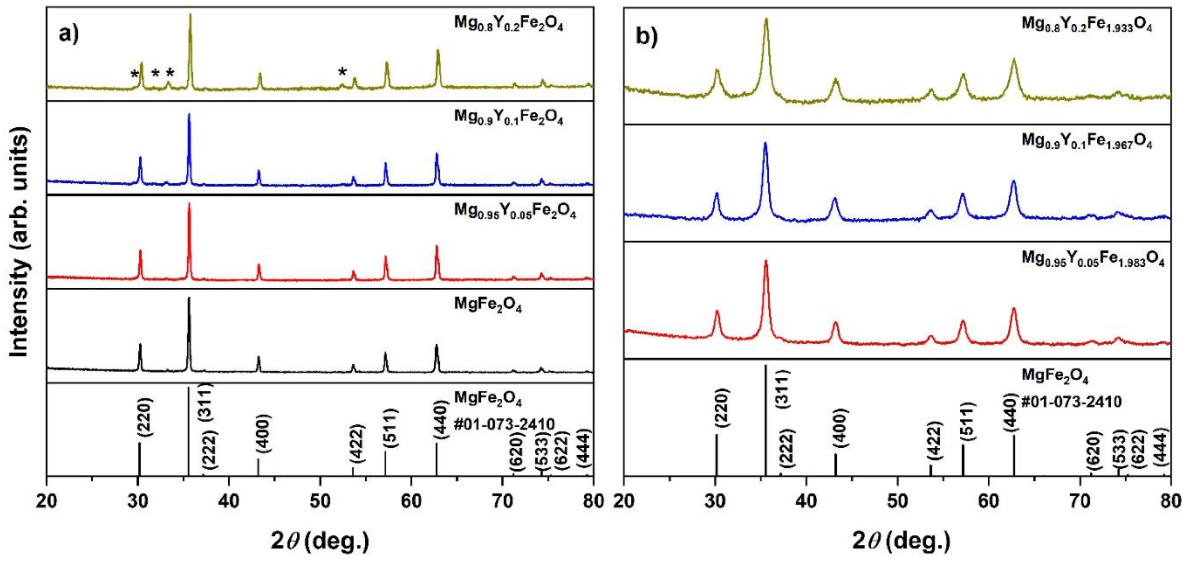

Fig. 3 X-ray diffraction patterns of $Mg_{1-x}Y_xFe_{2-\delta}O_4$ for $\delta = 0$ (a) and $\delta = x/3$ (b); asterisks mark $YFeO_3$ impurity peaks. Reproduced from Karoblis et al. [50] under the Creative Commons Attribution licence.

Table 2. Structural and microstructural data for Y-substituted hosts.

Host	Y range	Phase purity	Lattice / size data	Ref.

$Mg_{0.5}Zn_{0.5}Y_xFe_{2-x}O_4$	0–0.05	Single phase to x = 0.03; $YFeO_3$ at x ≥ 0.04	a_{expt}: 8.4309 Å (x = 0), 8.4366 Å (0.02), 8.4288 Å (0.05); bulk density 4.006 → 4.197 g/cm^3 (x = 0.02)	[48, 49]
$Mg_{1-x}Y_xFe_{2-\delta}O_4$, δ = 0	up to 0.2	$YFeO_3$ impurity, increasing with Y	–	[50]
$Mg_{1-x}Y_xFe_{2-\delta}O_4$, δ = x/3	up to 0.2	Single phase up to x = 0.2	Crystallite size ~40 nm → 10–13 nm	[50]
$NiFe_{2-x}Y_xO_4$	0.05–0.3	Secondary phase at x ≥ 0.15 (earlier study)	Grain size decreases with Y (attributed to pinning by secondary phases)	[46]
$Ni_{0.6}Zn_{0.3}Co_{0.1}Y_xFe_{2-x}O_4$	0–0.1	$YFeO_3$ for x > 0.025 (MST and CST)	–	[53]
$CuFe_{2-x}Y_xO_4$	0.1–0.5	Tetragonal Cu ferrite retained	–	[56]
$Y_{3-x}Ca_xFe_{5-x-y}In_ySn_xO_{12}$ (garnet)	x = 0.05–0.3	Single YIG phase in all samples	a = 12.425 → 12.463 Å (y = 0.45, x = 0.05 → 0.3)	[71]

Site occupancy is also host-dependent and should not be assumed. In Mg–Zn ferrite Y is argued to enter B sites [48], whereas in Mg ferrite the FTIR and Mössbauer data of Karoblis et al. were read as suggesting that Y^{3+} tends toward tetrahedral positions, with the amount of iron on tetrahedral sites increasing as Y was added [50]. In the garnet $Y_3Fe_5O_{12}$, Y^{3+} occupies the dodecahedral c sites by construction, and the magnetic moment arises from antiparallel Fe^{3+} on the a and d sites [71].

3.2. Microstrain, grain growth and density

Lattice distortion from the oversized Y^{3+} ion is linked in the literature to changes in anisotropy and domain-wall pinning, which are invoked to explain the coercivity increase in $Mg_{0.6}Zn_{0.4}Y_xFe_{2-x}O_4$ [3]. Microstructural responses differ between systems. In solid-state Mg–Zn ferrite the grain size grew from 1.22 μm to 3.65–3.75 μm at x = 0.01–0.02 and then shrank to 1.28 μm at x = 0.03, and the bulk density followed the same pattern [48]. In sol-gel Mg ferrite the individual particles became smaller with more Y while the aggregates became larger [50], and in co-precipitated Ni ferrite the grain size decreased with Y [46]. Studies of Y-doped Co-based hosts also report refined crystallite size [43, 72]. Microstructural conclusions should therefore be drawn per system, supported by Williamson–Hall or Rietveld analysis rather than assumed.

3.3. FTIR and Raman spectroscopy

Spinel ferrites show a higher-frequency band (about 550–600 cm^{-1}) assigned to tetrahedral M–O stretching and a lower-frequency band (about 400–450 cm^{-1}) assigned to octahedral M–O vibrations; both bands were confirmed in Y-substituted $MnFe_2O_4$ [7]. In Mg ferrite the bands lie near 565 and 406 cm^{-1}; with Y the lower band stayed put while the main band shifted slightly, which was one of the arguments for tetrahedral Y occupancy [50]. A heavier, larger ion changes the reduced mass and bond length, so band shifts and broadening are commonly

taken as evidence of altered cation distribution; this interpretation is qualitative and should be corroborated with refinement or Mössbauer data. Density functional theory has been combined with experiment for Y-doped $NiFe_2O_4$ to complement such assignments [47].

4. Tuning of Magnetic and Dielectric Properties

Y^{3+}-induced strain and site substitution are reflected in magnetic and electrical behavior (Table 3). The table shows that no single trend applies to all hosts.

4.1. Magnetic response and superexchange dilution

In Néel's two-sublattice picture the net moment is the difference between the octahedral and tetrahedral sublattice magnetizations. Replacing Fe^{3+} (5 μ_B) on B sites with diamagnetic Y^{3+} (0 μ_B) dilutes the B sublattice and weakens A–B exchange, so a decrease in saturation magnetization is the most common outcome. It is reported for Y-doped $MgFe_2O_4$ [50], Y-doped $CoFe_2O_4$ [44] and $Ni_{0.5}Zn_{0.3}Mn_{0.2}Y_xFe_{2-x}O_4$, where it fell from about 61 to 45 emu/g at x = 0.08 [73]. Y-doped Co–Zn ferrite has likewise been examined for transducer applications [74]. Weakened exchange is also consistent with the lower Curie temperature of Y-substituted Mg–Zn ferrite [49]. The trend is rarely monotonic, however. In $Mg_{0.5}Zn_{0.5}Y_xFe_{2-x}O_4$ the saturation magnetization fell from 63.7 emu/g to 50.1 emu/g at x = 0.02, recovered to 58.3 emu/g at x = 0.03, and then dropped to 40.1 and 46.8 emu/g at x = 0.04 and 0.05, a pattern attributed to Mg^{2+} migration and cation redistribution on top of simple dilution [48] (Fig. 4b). In $Ni_{0.5}Co_{0.5}Fe_{2-x}Y_xO_4$ ($x \leq 0.02$) the magnetization even increased from about 55 to 61 emu/g [52]. In combustion-synthesized $CoFe_2O_4$, Ms fell from 69 to 33 emu/g between x = 0 and 0.04 while the coercivity rose from 1100 to 1900 Oe [40], and sol-gel $BaY_yFe_{2-y}O_4$ likewise showed lower Ms and larger Hc with yttrium [66].

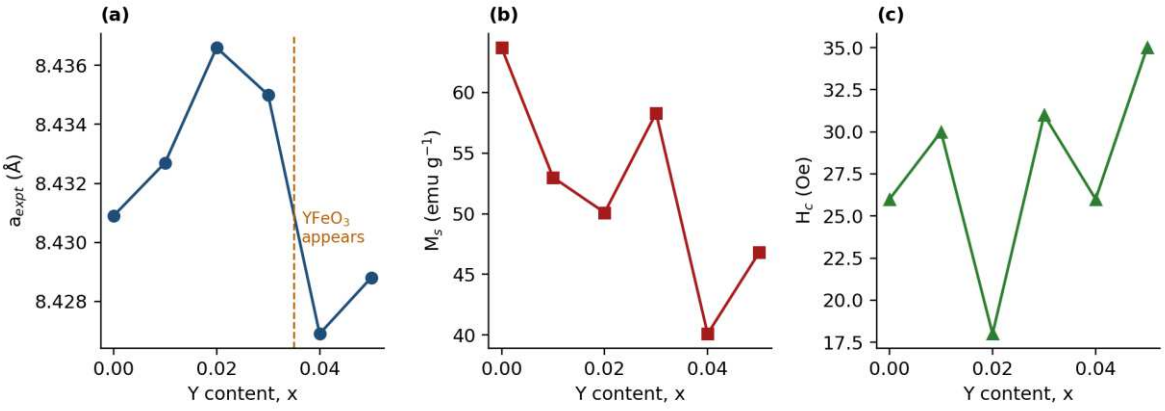

Fig. 4 Re-plotted tabulated data for $Mg_{0.5}Zn_{0.5}Y_xFe_{2-x}O_4$: (a) experimental lattice constant, (b) saturation magnetization and (c) coercivity versus Y content. Data from Ali et al. [48]; original plot prepared by the authors.

Part of the fall in magnetization may not be dilution at all. In the Mg ferrite study, the decrease of Ms (from 26 emu/g to 16 or 20 emu/g) and of Hc (from 70 Oe to 17 or 5 Oe) accompanied a drop in grain size, and the authors considered the growth of a magnetically disordered, “dead” intergranular layer the major factor; Mössbauer spectra showed a growing superparamagnetic fraction and an average hyperfine field reduced by up to 50% [50]. Coercivity is therefore especially host-dependent, rising with Y in cobalt and barium-based ferrites [40, 66] but falling in Mg ferrite [50]. In $Mg_{0.6}Zn_{0.4}Y_xFe_{2-x}O_4$ it increased and the remanent magnetization stayed nearly constant, which was attributed to enhanced anisotropy, lattice strain and domain-wall pinning [3], while Mg–Zn ferrite made by the ceramic route stayed soft (18–35 Oe) without a monotonic trend [48]. Soft behavior with low coercivity and high resistivity has been emphasized for Y-substituted Ni–Zn–Co ferrite [53]. “Magnetic softening” is thus a host-specific outcome and not a general property of yttrium. Garnets illustrate the same principle with different cations: in Ca–In–Sn co-substituted YIG, Ms decreased as the substitution increased and Hc reached 0.95 Oe, with the resonance linewidth set by anisotropy and porosity contributions [71]. Unlike Sm^{3+} or Dy^{3+}, Y^{3+} has no 4f electrons, so any 3d–4f coupling picture applies to those lanthanides [35, 36] and not to yttrium; Y acts through dilution, strain, grain-size effects and cation redistribution.

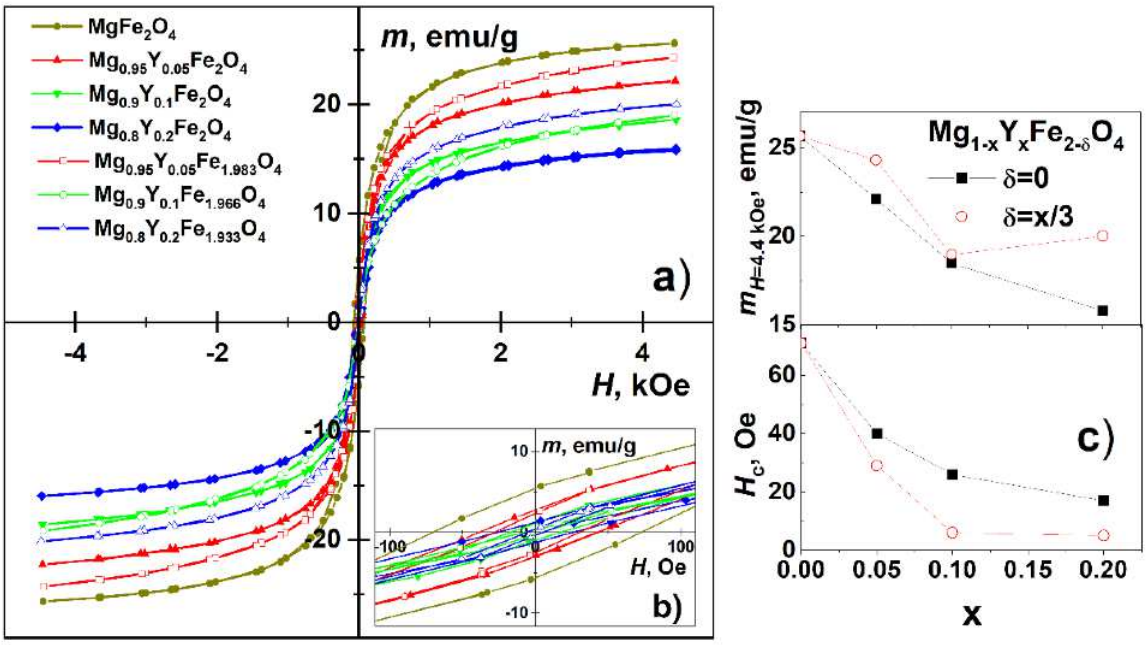

Fig. 5 Magnetization hysteresis loops of $Mg_{1-x}Y_xFe_{2-\delta}O_4$ and the corresponding saturation magnetization and coercivity. Reproduced from Karoblis et al. [50] under the Creative Commons Attribution licence.

Table 3. Reported magnetic and electrical/dielectric trends for Y-substituted hosts.

Host	Magnetic trend	Electrical / dielectric trend	Ref.
$Mg_{0.6}Zn_{0.4}Y_xFe_{2-x}O_4$	Hc increases (anisotropy, strain, domain-wall pinning); Mr nearly unchanged	AC conductivity dispersion explained by Maxwell–Wagner interfacial polarization	[3]
Y-doped $MgFe_2O_4$	Ms 26 → 16 (δ = 0) or 20 emu/g (δ = x/3); Hc 70 → 17 or 5 Oe	–	[50]
$Mg_{0.5}Zn_{0.5}Y_xFe_{2-x}O_4$	Ms 63.7 → 50.1 (x = 0.02), 58.3 (0.03), 40.1 (0.04), 46.8 emu/g (0.05); Hc 18–35 Oe; Tc decreases	AC resistivity rises from ~10^5 to ~10^6 Ω cm at 20 Hz for x ≥ 0.02–0.04; ε′ lowered; relaxation time 15–31 ns	[48, 49]
$Ni_{0.5}Co_{0.5}Fe_{2-x}Y_xO_4$	Ms increases (~55 to ~61 emu/g)	–	[52]
$Ni_{0.5}Zn_{0.3}Mn_{0.2}Y_xFe_{2-x}O_4$	Ms decreases (~61 to ~45 emu/g at x = 0.08); low-coercivity composition reported	–	[73]
Y-doped $CoFe_2O_4$	Ms 69 → 33 emu/g and Hc 1100 → 1900 Oe (x = 0 → 0.04); Ms decreases in sol-gel samples	Dielectric relaxation and charge-carrier dynamics modified; maximum conductivity at 15 mol% Y in a citrate-route series	[40–42, 44]
$BaY_yFe_{2-y}O_4$	Ms decreases; Hc increases	Resistivity, activation energy and bond length increase	[66]
$CuFe_{2-x}Y_xO_4$	–	Real permittivity ~5 to ~3 and real permeability ~2.5 to ~1.75 (relative values) over 1–6 GHz as Y increases	[56]
$NiFe_{2-x}Y_xO_4$ (x = 0.05, 0.15, 0.3)	–	Grain/grain-boundary conduction (E_a ≈ 0.3 eV for grains); conductivity rises at x = 0.05 and falls at higher x; ε′ maximal at x = 0.15	[46]
Y-substituted $MnFe_2O_4$	–	Dielectric properties modified; lattice constant increases	[7]
$Y_{3-x}Ca_xFe_{5-x-y}In_ySn_xO_{12}$	Ms decreases with substitution; Hc as low as 0.95 Oe; ΔH = 29 Oe	–	[71]
Y,Co co-doped $BiFeO_3$	Magnetic and magneto-dielectric behavior modified	Electrical properties modified	[75]

4.2. Dielectric dispersion and charge-carrier dynamics

Conduction in ferrites is usually ascribed to $Fe^{2+}\leftrightarrow Fe^{3+}$ hopping on octahedral sites. The Maxwell–Wagner two-layer picture, in which conducting grains are separated by resistive grain boundaries, accounts for the high low-frequency permittivity and its dispersion, as invoked for $Mg_{0.6}Zn_{0.4}Y_xFe_{2-x}O_4$ [3] and Y-doped $NiFe_2O_4$ [46]. Since Y^{3+} replaces Fe^{3+} on B sites, it removes hopping pairs, and substituted Mg–Zn ferrites showed about an order-of-magnitude rise in resistivity together with lower dielectric constant [48]. The effect depends on concentration: in Ni ferrite the conductivity increased at x = 0.05, where the hopping distance shortens, and decreased at larger x, where the loss of Fe^{2+}–Fe^{3+} pairs and the larger separation dominate [46]. Related reductions in permittivity or modified relaxation have been reported for Y-doped $CoFe_2O_4$ [42] and $MnFe_2O_4$ [7], and in a citrate-route $CoFe_2O_4$ series the electrical conductivity peaked at 15 mol% Y rather than changing monotonically [41]. At microwave frequency, $CuFe_{2-x}Y_xO_4$ showed reductions of real permittivity from about 5 to 3 and real permeability from about 2.5 to 1.75 over 1–6 GHz [56]. These are relative (dimensionless)

quantities and the original report's "F/m" and "H/m" labels should not be used. Different hosts, frequency windows and measurement protocols mean that dielectric numbers from different papers cannot be compared directly.

A set of complementary analysis tools is used across these studies (Table 4). Impedance and modulus spectra separate grain and grain-boundary contributions, constant phase elements describe non-ideal capacitance, and Jonscher-type power laws describe the ac conductivity [46, 48]. The same formalisms are applied to other oxides, including Zn-, Co- and Mn-doped ferrites [76, 77], RE-doped titanates [78, 79], Sm-doped lead titanate–ferrite ceramics [80] and spinel $NiCo_2O_4$ [81], and they transfer directly to Y-substituted spinels.

Table 4. Dielectric and impedance analysis methods used for doped ferrites and related oxides.

Method	What it provides	Example material	Ref.
Impedance spectroscopy with constant phase element	Grain and grain-boundary contributions; non-ideal (Cole–Cole) behavior; relaxation times and activation energies	Y-doped $NiFe_2O_4$	[46]
Jonscher power law, Koops / Maxwell–Wagner model	Frequency dependence of ac conductivity and permittivity; two-layer (grain / boundary) picture	Mg–Zn–Y ferrite	[3, 48]
Electric modulus analysis	Transition from long- to short-range carrier mobility; relaxation time	Mg–Zn–Y ferrite; Er-doped titanate	[48, 78]
Dopant-dependent dielectric relaxation	Tuning of relaxation by cation type and content	$M_xCo_{1-x}Fe_2O_4$	[76]
Complex impedance, nanocrystalline vs bulk	Size-dependent transport	$NiFe_2O_4$	[77]
Non-Debye relaxation analysis	Distribution of relaxation times	Sm-doped $PbTiO_3$-based ceramic	[80]
Structural + dielectric correlation for RE doping	Role of RE content in dielectric response	$Bi_{3-x}Nd_xTi_{1.5}W_{0.5}O_9$	[79]
Electrical transport in spinel oxides	Conduction mechanism of a spinel electrode material	$NiCo_2O_4$	[81]

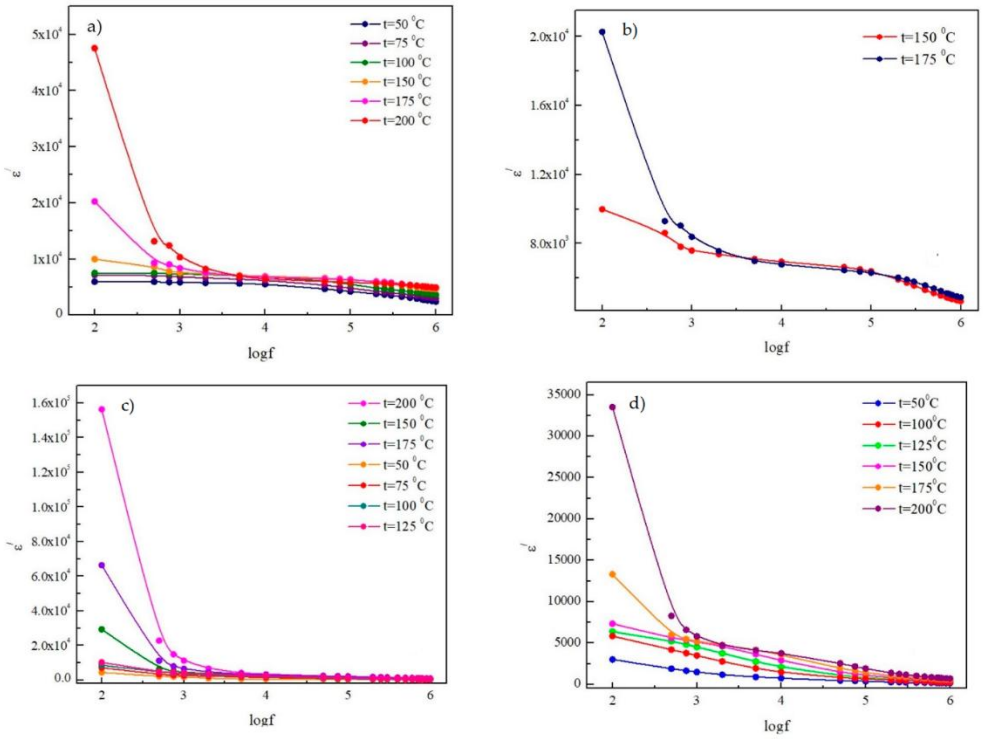

Fig. 6 Frequency dependence of the real part of the dielectric permittivity of $NiFe_{2-x}Y_xO_4$ nanopowders. Reproduced from Šiljegović et al. [46] under the Creative Commons Attribution licence.

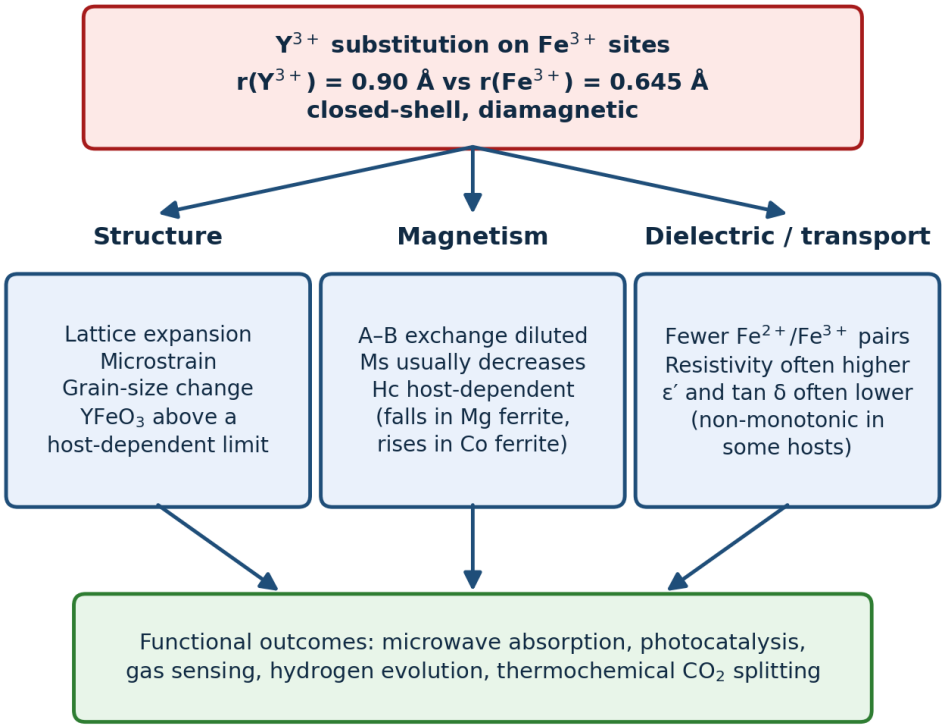

Fig. 7 Conceptual summary of the effects of Y^{3+} substitution on structure, magnetism and dielectric behavior and the resulting functional outcomes (original illustration prepared by the authors; trends are those compiled in Tables 1–3).

5. Advanced and Emerging Applications

The structural and charge-transport changes above underpin the applications compiled in Table 5.

Table 5. Representative applications of Y-modified magnetic oxides.

Application	Material	Reported result	Ref.
Microwave absorption / EMI	$CuFe_{2-x}Y_xO_4$	Real permittivity and permeability decrease over 1–6 GHz; suitable for radar and shielding use	[56]
Microwave absorption	$Co_{0.5}Ni_{0.5}Y_xFe_{2-x}O_4$ (hydrothermal)	Evaluated for X-band absorption, $0 \le x \le 1.0$	[65]
Microwave devices	$Ni_{0.6}Zn_{0.3}Co_{0.1}Y_xFe_{2-x}O_4$	MST samples outperform CST; low coercivity and high resistivity	[53]
Microwave / magnetic	Mg,Y co-doped $MnFe_2O_4$	Superparamagnetic particles proposed for magnetic and microwave applications	[37]
Photocatalysis	Co/Y co-doped $Ni_{0.6}Mg_{0.4}Fe_2O_4$	Solar-light degradation of organic dyes	[23]
Photocatalysis	Y-doped $CoFe_2O_4$	Photocatalytic activity linked to modified optical and magnetic properties	[43]
Catalysis	Y-doped $CoFe_2O_4$	Catalytic performance boosted by Y^{3+} inclusion	[39]
Photocatalysis	Y-substituted Co–Cu–Zn ferrite	Enhanced physical properties and photocatalysis	[72]
Photocatalysis	Y/Sn co-doped $BiFeO_3$ 2D nanoplates	Degradation of cationic dyes	[69]
Adsorption	$Y_{0.045}Ni_{0.045}Fe_{2.91}O_4$ nanowires on mesoporous silica	Crystal violet removal (RSM, kinetics, isotherms)	[70]
Gas sensing	Y-doped $NiFe_2O_4$ and $ZnFe_2O_4$ nanofibers	Enhanced sensing with rapid response; n-butanol sensor	[67, 68]
Electrocatalysis (HER)	$NiFe_{2-(x+y)}Y_xCe_yO_4$	Lowest Tafel slope 80 mV dec^{-1} in 1 M KOH	[57]
Thermochemical CO_2 splitting	Y-containing $CoFe_2O_4$	Enhanced performance in two-step cycle	[82]
Magneto-dielectric	Y,Co co-doped $BiFeO_3$	Electrical, magnetic and magneto-dielectric properties investigated	[75]

5.1. High-frequency electronics and electromagnetic absorption

Pristine ferrites can show impedance mismatch and loss at gigahertz frequencies, and Y^{3+} offers a way to adjust complex permittivity and permeability. Spinel ferrites and their composites for microwave absorption have been reviewed [17], including $MgFe_2O_4$/RGO absorbers [18]. In $CuFe_{2-x}Y_xO_4$ the magneto-dielectric properties were considered suitable for radar and shielding applications [56]. Hydrothermally prepared $Co_{0.5}Ni_{0.5}Y_xFe_{2-x}O_4$ was evaluated as an X-band (8–12 GHz) microwave absorber [65], and microwave-sintered $Ni_{0.6}Zn_{0.3}Co_{0.1}Y_xFe_{2-x}O_4$ showed improved electromagnetic properties relative to conventionally sintered samples [53]. Mg and Y co-doped superparamagnetic $MnFe_2O_4$ was proposed for magnetic and microwave applications [37]. In Mg–Zn ferrite the enhanced resistivity, reduced dielectric constant and low coercivity were judged suitable for high-frequency devices [48].

5.2. Visible-light photocatalysis and water remediation

Doping with Y^{3+} has been used to modify optical absorption and photocatalytic or catalytic activity. Examples include solar-light degradation of organic dyes by Co/Y co-doped $Ni_{0.6}Mg_{0.4}Fe_2O_4$ [23], Y-doped $CoFe_2O_4$ [39, 43], Y-substituted Co–Cu–Zn ferrite [72], and Y/Mn co-modified cobalt ferrites that were also tested for biological activity [55]. Lanthanide-doped Mg ferrite has been used for methylene blue degradation on Fenton-like catalysts [51]. The effect on the band gap depends on host and defect chemistry and is not universally a narrowing, so claims should be based on measured band-gap data for each system. Low-dimensional and perovskite-type systems extend this work: Y/Sn co-doped $BiFeO_3$ nanoplates for cationic dye degradation [69], Gd/Sn co-doped $BiFeO_3$ as a solar-light photocatalyst [83], Y-doped $LaFeO_3$ for dye degradation [4], and Y–Ni–Fe oxide nanowires on mesoporous silica for crystal violet removal [70]. Ni-substituted $MgFe_2O_4$ was also examined for photocatalytic applications [63].

5.3. Electrocatalysis and thermochemical conversion

In $NiFe_{2-(x+y)}Y_xCe_yO_4$ prepared by solution combustion, Y/Ce co-doping improved hydrogen-evolution activity in 1 M KOH, and the best composition reached a Tafel slope of 80 mV dec^{-1} [57]. Y-containing $CoFe_2O_4$ has also been reported to improve performance in two-step thermochemical CO_2 splitting [82].

Two-step thermochemical cycles reduce a metal oxide at high temperature and re-oxidize it with CO_2 or H_2O, and perovskites, ceria and ferrites are leading redox materials [84–87]. Data from different laboratories must be compared with care. In a controlled comparison under one protocol, 10% B-site substitution of $La_{0.7}Sr_{0.3}MnO_3$ by Mg, Ni or Co raised the O_2 and CO productivities by roughly 1.3–1.4 times (for example from 143 and 248 μmol g^{-1} to 197 and 354 μmol g^{-1} for Mg), Cu substitution led to irreversible decomposition, and the Mg-substituted material lost only 4.3% of its O_2 and 1.0% of its CO productivity over 50 cycles [88] (Fig. 8a, Table 6). Yttrium itself shows route-dependent behavior: $Y_{0.5}Sr_{0.5}MnO_3$ outperformed $La_{0.5}Sr_{0.5}MnO_3$ when made by a solid-state route [89] but underperformed it when made by solution combustion [90] (Fig. 8b). Other lanthanide and B-site substitutions in perovskites and ceria have been surveyed in similar fashion [91–97]. The authors of the comparison also caution that thermogravimetric productivities can overestimate yields relative to direct gas analysis, which argues for standardized benchmarking [88, 98].

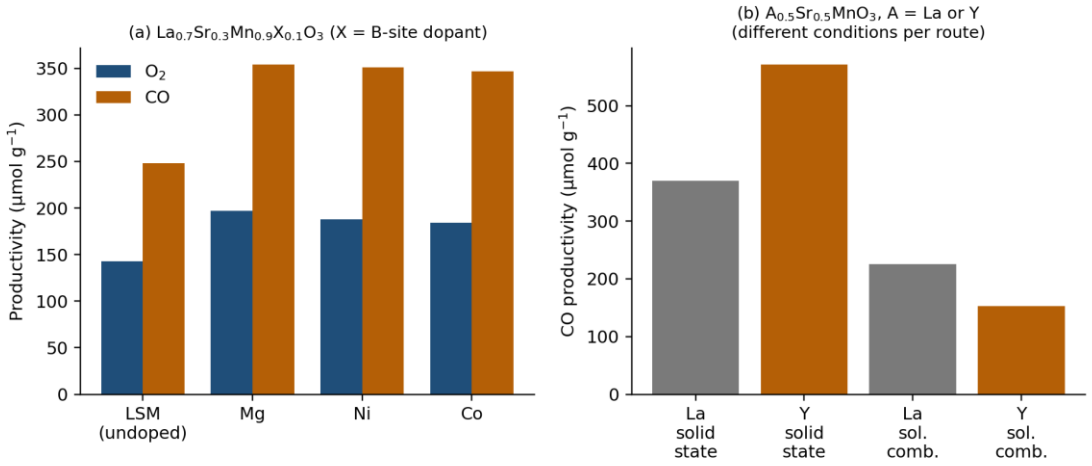

Fig. 8 (a) O_2 and CO productivities of $La_{0.7}Sr_{0.3}Mn_{0.9}X_{0.1}O_3$ under one protocol, and (b) CO productivity of $Y_{0.5}Sr_{0.5}MnO_3$ versus $La_{0.5}Sr_{0.5}MnO_3$ prepared by two routes under different conditions. Data compiled from Sawaguri et al. [88], who tabulated the results of [89, 90]; original plot prepared by the authors.

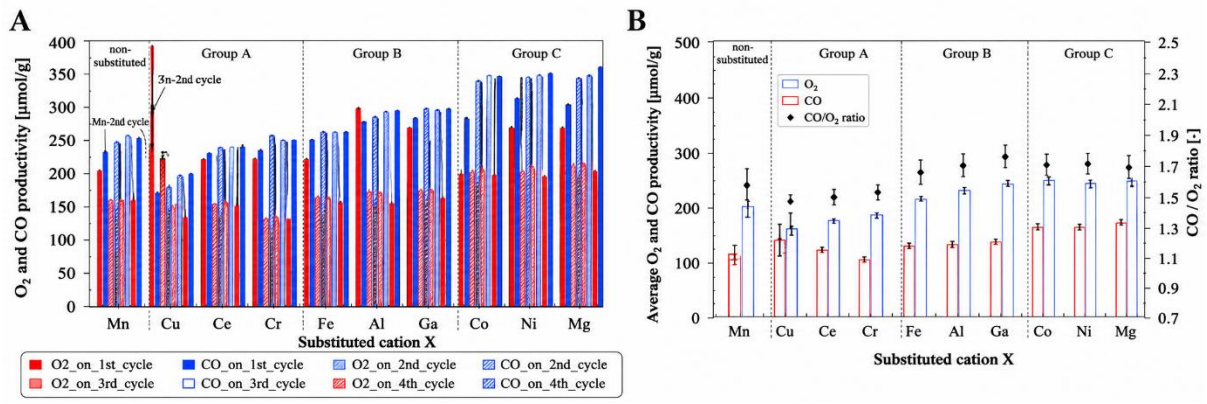

Fig. 9 O_2 and CO productivities of $La_{0.7}Sr_{0.3}Mn_{0.9}X_{0.1}O_3$ in two-step thermochemical CO_2 splitting. Reproduced from Sawaguri et al. [88] under the Creative Commons Attribution licence.

Table 6. Redox productivities in two-step thermochemical CO_2 splitting (thermogravimetric tests) for selected perovskites.

Material (route)	Conditions (reduction / oxidation)	O_2 (µmol/g)	CO (µmol/g)	Ref.
$La_{0.7}Sr_{0.3}MnO_3$ (Pechini)	1400 °C, 90 min / 1200 °C, 30 min	143	248	[88]
$La_{0.7}Sr_{0.3}Mn_{0.9}Mg_{0.1}O_3$	as above	197	354	[88]
$La_{0.7}Sr_{0.3}Mn_{0.9}Ni_{0.1}O_3$	as above	188	351	[88]
$La_{0.7}Sr_{0.3}Mn_{0.9}Co_{0.1}O_3$	as above	184	347	[88]
$Y_{0.5}Sr_{0.5}MnO_3$ (solid state)	1400 °C, 45 min / 1100 °C, 60 min	481	571	[89]
$La_{0.5}Sr_{0.5}MnO_3$ (solid state)	as above	198	370	[89]
$Y_{0.5}Sr_{0.5}MnO_3$ (solution combustion)	1400 °C, 60 min / 1000 °C, 60 min	87	153	[90]
$La_{0.5}Sr_{0.5}MnO_3$ (solution combustion)	as above	128	225	[90]

Note: Values as tabulated by Sawaguri et al. [88]; entries from different laboratories were measured under different conditions and are not directly comparable.

5.4. Gas sensing

Electrospun Y-doped $NiFe_2O_4$ nanofibers gave improved gas-sensing performance with a rapid response [67], and Y-doped $ZnFe_2O_4$ nanofibers were reported as an n-butanol sensor [68]. Nanofibrous morphologies and doping-induced defects are plausible contributors, but their individual roles need controlled experiments.

5.5. Garnet, perovskite and orthoferrite hosts

Because yttrium is also a structural constituent of garnets and orthoferrites, its role differs in these hosts (Table 7). In YIG, cations such as Ca, In, Sn, Zn, Zr, Ge, La, Pr and Bi are introduced to lower the ferromagnetic resonance linewidth and dielectric loss for microwave devices [71, 99–102], and rare-earth or Al substitution in YIG has been probed by NMR [5, 6]. In Ba-based hexaferrite and spinel systems, Y and other lanthanides alter electrical and magnetic properties [54, 66]. The $YMnO_3$ study of Gd substitution is a reminder that Y-containing hosts can themselves be tuned by substitution [103].

Table 7. Y-containing and Y-doped garnet, perovskite and related hosts.

Host	Focus reported	Type	Ref.
$Y_{3-x}Ca_xFe_{5-x-y}In_ySn_xO_{12}$	Single phase; ΔH = 29 Oe; Hc 0.95 Oe; mechanisms of linewidth	Garnet	[71]
La-, Pr-, Bi-substituted YIG	Magnetic behavior and characterization	Garnet	[99]
Ca–Sn co-substituted YIG	Thermomagnetization and FMR linewidth broadening	Garnet	[100]
Zn–Zr co-doped YIG	Structural, morphological, dielectric and magnetic properties	Garnet	[101]
Ca–Ge co-substituted YInIG	Low dielectric loss and narrow FMR linewidth	Garnet	[102]
Al, Nd substituted YIG; Sm, Nd garnets; Ni-YIG	NMR, magnetic and optical properties, annealing effects	Garnet	[5, 6, 60]
Y (A site) and Ni (B site) doped $LaFeO_3$	Photocatalytic dye degradation	Perovskite	[4]
Y,Co co-doped $BiFeO_3$; Y/Sn co-doped $BiFeO_3$	Magneto-dielectric properties; cationic dye degradation	Perovskite	[69, 75]
Gd-substituted $YMnO_3$	Substitution effects in hexagonal Y manganite	Manganite	[103]
Gd–Sm–Y doped barium hexaferrite	Structural, magnetic and DFT investigation	Hexaferrite	[54]
Y-doped Ba-based spinel ferrite	Electrical and magnetic properties	Spinel	[66]
$A_{0.5}Sr_{0.5}MnO_3$ (A includes Y)	Thermochemical CO_2 splitting	Perovskite	[90]

6. Future Perspectives and Unresolved Challenges

Several issues limit comparison between studies and deserve attention. First, the literature does cover wide composition ranges, from x = 0.3 in Mg–Zn ferrite [3] and 20 mol% in Mg ferrite [50] to x = 1.0 in Co–Ni ferrite [65]. The gap is therefore not a lack of high-Y samples but the lack of consistent phase-purity, stoichiometry and site-occupancy characterization across them. Reporting of the iron compensation used, quantitative phase fractions of $YFeO_3$, and Rietveld or Mössbauer determination of site occupancy [50] should become standard. Co-substitution

at the A site of Y-doped spinels is another route to tune structural, optical, electrical and magnetic properties [104].

Second, the opposite coercivity and magnetization trends in different hosts [3, 50, 52] call for systematic studies in which host composition, route and thermal history are varied independently, and in which grain size is controlled so that dilution can be separated from finite-size effects [48, 50]. Third, dielectric and microwave data should be reported as relative quantities with explicit frequency windows and sample geometry, as the unit errors in some reports show, and should use common impedance and modulus formalisms [46, 76]. Fourth, computational work could help separate dilution, strain and cation-redistribution effects; density functional theory has already been combined with experiment for Y-doped $NiFe_2O_4$ [47] and co-doped hexaferrites [54] and could be extended to Y-substituted spinels. Fifth, thermochemical redox data need standardized benchmarking because productivities depend strongly on protocol and method of gas quantification [88, 98]. Finally, translating powder-level performance into films and devices (sensors, electrodes, absorbers) requires demonstration of stability and reproducibility, and, for dual-doped systems such as Y/Ce or Y/Sn, of the specific contribution of yttrium relative to the co-dopant [57, 69].

7. Conclusion

Yttrium substitution is a versatile but host-dependent tool for engineering magnetic oxides. Its large ionic radius and closed-shell, non-magnetic character generally lead to lattice expansion, strain and dilution of A–B superexchange, so saturation magnetization usually decreases, although increases and non-monotonic behavior have been reported and part of the decrease reflects grain-size effects. Coercivity may decrease (Mg ferrite) or increase (cobalt and barium-based ferrites), and the amount of Y^{3+} accepted before $YFeO_3$ forms ranges from about x = 0.025 to 20 mol% depending on host, route and iron compensation. Reduced hopping on octahedral sites often raises resistivity and lowers permittivity and dielectric loss, which supports use in high-frequency devices, although at low Y content the conductivity can rise. These changes underpin reported benefits in microwave absorption, photocatalysis, gas sensing, electrocatalytic hydrogen evolution and thermochemical CO_2 splitting, where yttrium's effect is itself route-dependent. Progress now depends less on exploring new compositions than on rigorous, comparable characterization of phase purity, stoichiometry, site occupancy and dielectric response, together with device-level validation.

Declarations

Acknowledgments: The authors sincerely thank the PG & Research Department of Physics at St. Joseph's College of Arts and Science (Autonomous), Cuddalore-607001, affiliated with Annamalai University, India, for providing the essential library resources.

Third party material: Not applicable.

Ethical approval: Not applicable.

Informed consent: Not applicable.

Data availability: Not applicable.

Conflict of interest: The authors declare no financial or non-financial interests directly or indirectly related to the submitted work.

References

1. Zahoor I, Irfan M, Jamil A, Castegnaro MV, Rasool RT, Gulbadan S, et al (2025) Synergistic structural integrity and opto-dielectric response of Y^{3+}-modified Co-Mg-Fe-O system. Ceram Int 51:53822–53836. https://doi.org/10.1016/j.ceramint.2025.09.126
2. Sarfraz Z, Hussain M, Luqman M, Akram R (2024) Synthesis, structural characterization, and frequency dependent dielectric analysis of cobalt-doped magnesium ferrite nanoparticles for advanced energy storage systems. Mater Sci Eng B 310:117780. https://doi.org/10.1016/j.mseb.2024.117780
3. Bindushree BM, Chavan G, Naik LR, Bhajantri RF, Gudihal V (2025) Effect of yttrium doping on the physical properties of Mg-Zn ferrite: a detailed study. Next Mater 9:101247. https://doi.org/10.1016/j.nxmate.2025.101247
4. Sultan H, Sultan A, Abdellatief M, Tayyaba Q, Gul M, Ali T (2024) Photocatalytic activity (dye degradation) of pristine and doped $LaFeO_3$ (dopant Y at A site and Ni at B site) by impedance spectroscopy. Ceram Int 50(21):44303–44315. https://doi.org/10.1016/j.ceramint.2024.08.279
5. Georgi AD, Reddy GS, Ramesh KP, Mallikarjunaiah KJ (2024) Effect of substitution of aluminium and neodymium on structural and magnetic properties of yttrium iron garnet studied using ^{57}Fe internal field NMR. Solid State Sci 156:107658. https://doi.org/10.1016/j.solidstatesciences.2024.107658
6. Yousaf M, Noor A, Xu S, Akhtar MN, Wang B (2020) Magnetic characteristics and optical band alignments of rare-earth (Sm^{3+}, Nd^{3+}) doped garnet ferrite nanoparticles (NPs). Ceram Int 46(10):16524–16532. https://doi.org/10.1016/j.ceramint.2020.03.219
7. Yousuf MA, Baig MM, Al-Khalli NF, Khan MA, Aboud MFA, Shakir I, Warsi MF (2019) The impact of yttrium cations (Y^{3+}) on structural, spectral and dielectric properties of spinel manganese ferrite nanoparticles. Ceram Int 45(8):10936–10942. https://doi.org/10.1016/j.ceramint.2019.02.174

8. Kudr J, Haddad Y, Richtera L, Heger Z, Cernak M, Adam V, Zitka O (2017) Magnetic nanoparticles: from design and synthesis to real world applications. Nanomaterials 7:243. https://doi.org/10.3390/nano7090243

9. Zhao S, Yu X, Qian Y, Chen W, Shen J (2020) Multifunctional magnetic iron oxide nanoparticles: an advanced platform for cancer theranostics. Theranostics 10:6278–6309. https://doi.org/10.7150/thno.42564

10. Selim MM, El-Safty S, Tounsi A, Shenashen M (2024) A review of magnetic nanoparticles used in nanomedicine. APL Mater 12:010601. https://doi.org/10.1063/5.0191034

11. Amiri M, Salavati-Niasari M, Akbari A (2019) Magnetic nanocarriers: evolution of spinel ferrites for medical applications. Adv Colloid Interface Sci 265:29–44. https://doi.org/10.1016/j.cis.2019.01.003

12. Kefeni KK, Msagati TAM, Nkambule TTI, Mamba BB (2020) Spinel ferrite nanoparticles and nanocomposites for biomedical applications and their toxicity. Mater Sci Eng C 107:110314. https://doi.org/10.1016/j.msec.2019.110314

13. Shahjuee T, Masoudpanah SM, Mirkazemi SM (2019) Thermal decomposition synthesis of $MgFe_2O_4$ nanoparticles for magnetic hyperthermia. J Supercond Nov Magn 32:1347–1352. https://doi.org/10.1007/s10948-018-4834-1

14. Ivanets A, Prozorovich V, Roshchina M, Grigoraviciute-Puroniene I, Zarkov A, Kareiva A, et al (2020) Heterogeneous Fenton oxidation using magnesium ferrite nanoparticles for ibuprofen removal from wastewater: optimization and kinetics studies. J Nanomater 2020:8159628. https://doi.org/10.1155/2020/8159628

15. Sharma L, Kakkar R (2018) Magnetically retrievable one-pot fabrication of mesoporous magnesium ferrite ($MgFe_2O_4$) for the remediation of chlorpyrifos and real pesticide wastewater. J Environ Chem Eng 6:6891–6903. https://doi.org/10.1016/j.jece.2018.10.058

16. Jiang Z, Chen K, Zhang Y, Wang Y, Wang F, Zhang G, Dionysiou DD (2020) Magnetically recoverable $MgFe_2O_4$/conjugated polyvinyl chloride derivative nanocomposite with higher visible-light photocatalytic activity for treating Cr(VI)-polluted water. Sep Purif Technol 236:116272. https://doi.org/10.1016/j.seppur.2019.116272

17. Xie X, Wang B, Wang Y, Ni C, Sun X, Du W (2022) Spinel structured MFe_2O_4 (M = Fe, Co, Ni, Mn, Zn) and their composites for microwave absorption: a review. Chem Eng J 428:131160. https://doi.org/10.1016/j.cej.2021.131160

18. Heidari P, Masoudpanah SM (2020) A facial synthesis of $MgFe_2O_4$/RGO nanocomposite powders as a high performance microwave absorber. J Alloys Compd 834:155166. https://doi.org/10.1016/j.jallcom.2020.155166

19. Nayak S, Nayak SS, Kittur AA, Nayak S, Joshi DR (2024) Synthesis, fabrication, and performance evaluation of lanthanum doped nickel cobalt ferrite electrode for supercapacitors in energy storage applications. J Energy Storage 101:113918. https://doi.org/10.1016/j.est.2024.113918

20. Khasim S, Pasha A, Ramakrishna BN, Prasad BS (2024) Facile synthesis of samarium (Sm^{3+}) doped cobalt-iron oxide nano ferrite as an advanced electrode material for possible supercapacitor applications. Mater Chem Phys 325:129675. https://doi.org/10.1016/j.matchemphys.2024.129675

21. Uke SJ, Mardikar SP, Bambole DR, Kumar Y, Chaudhari GN (2020) Sol-gel citrate synthesized Zn doped $MgFe_2O_4$ nanocrystals: a promising supercapacitor electrode material. Mater Sci Energy Technol 3:446–455. https://doi.org/10.1016/j.mset.2020.02.009

22. Ali NA, Idris NH, Din MFM, Mustafa NS, Sazelee NA, Yap FAH, et al (2018) Nanolayer-like-shaped $MgFe_2O_4$ synthesised via a simple hydrothermal method and its catalytic effect on the hydrogen storage properties of MgH_2. RSC Adv 8:15667–15674. https://doi.org/10.1039/C8RA02168F

23. Tony A, Verjhula A (2024) Solar light-mediated photocatalytic degradation of noxious organic dyes by Co^{2+} and Y^{3+} co-doped $Ni_{0.6}Mg_{0.4}Fe_2O_4$ spinel nanoferrites. Ceram Int 50:54099–54115. https://doi.org/10.1016/j.ceramint.2024.10.267 [author names to be confirmed against the publisher record]

24. Kaur H, Singh A, Kumar V, Ahlawat DS (2019) Structural, thermal and magnetic investigations of cobalt ferrite doped with Zn^{2+} and Cd^{2+} synthesized by auto combustion method. J Magn Magn Mater 474:505–511. https://doi.org/10.1016/j.jmmm.2018.11.010

25. Naik AB, Naik PP, Hasolkar SS, Naik D (2020) Structural, magnetic and electrical properties along with antifungal activity and adsorption ability of cobalt doped manganese ferrite nanoparticles synthesized using combustion route. Ceram Int 46:21046–21055. https://doi.org/10.1016/j.ceramint.2020.05.177

26. Abushad M, Arshad M, Naseem S, Ahmed H, Ansari A, Chakradhary VK, et al (2022) Synthesis and role of structural disorder on the optical, magnetic and dielectric properties of Zn doped $NiFe_2O_4$ nanoferrites. J Mol Struct 1253:132205. https://doi.org/10.1016/j.molstruc.2021.132205

27. Suresh J, Trinadh B, Babu BV, Reddy P, Mohan BS, Krishna AR, Samatha K (2021) Evaluation of micro-structural and magnetic properties of nickel nano-ferrite and Mn^{2+} substituted nickel nano-ferrite. Phys B Condens Matter 620:413264. https://doi.org/10.1016/j.physb.2021.413264

28. Phor L, Chahal S, Kumar V (2020) Zn^{2+} substituted superparamagnetic $MgFe_2O_4$ spinel-ferrites: investigations on structural and spin-interactions. J Adv Ceram 9:576–587. https://doi.org/10.1007/s40145-020-0396-3

29. Wang X, Kan X, Liu X, Feng S, Zheng G, Cheng Z, et al (2020) Characterization of microstructure and magnetic properties for Co^{2+} ions doped $MgFe_2O_4$ spinel ferrites. Mater Today Commun 25:101414. https://doi.org/10.1016/j.mtcomm.2020.101414

30. Varma MC, Bharadwaj S, Choudary GSVRK, Murthy KSR, Rao KH (2017) Influence of magnesium-substituted Ni–Zn ferrites on magnetic and electric losses at lower frequency. Int J Mod Phys B 31:1750063. https://doi.org/10.1142/S0217979217500631

31. Chintala JNPK, Varma MC, Choudary GSVRK, Rao KH (2021) Control of coercivity and magnetic anisotropy through cobalt substitution in Ni-Zn ferrite. J Supercond Nov Magn 34:2357–2370. https://doi.org/10.1007/s10948-021-05965-0

32. Gangaswamy DRS, Choudary GSVRK, Varma MC, Bharadwaj S, Rao KH (2018) Enhanced magnetic permeability in $Ni_{0.55-y}Co_yZn_{0.35}Mg_{0.10}Fe_2O_4$ synthesized by sol-gel method. J Supercond Nov Magn 31:3753–3760. https://doi.org/10.1007/s10948-018-4638-3

33. Vinnik DA, Sherstyuk DP, Zhivulin VE, Zhivulin DE, Starikov AY, Gudkova SA, et al (2022) Impact of the Zn–Co content on structural and magnetic characteristics of the Ni spinel ferrites. Ceram Int 48:18124–18133. https://doi.org/10.1016/j.ceramint.2022.03.070

34. Dippong T, Levei EA, Cadar O, Deac IG, Lazar M, Borodi G, Petean I (2020) Effect of amorphous SiO_2 matrix on structural and magnetic properties of $Cu_{0.6}Co_{0.4}Fe_2O_4/SiO_2$ nanocomposites. J Alloys Compd 849:156695. https://doi.org/10.1016/j.jallcom.2020.156695

35. Zhang J, Mu X, Zhang Q, Poddubnaya N, Filippov D, Tao J, et al (2024) Structural, micro-structure, magnetic and dynamic magneto-elastic properties of samarium-doped nickel-zinc spinel ferrites for efficient power conversion applications. J Magn Magn Mater 602:172176. https://doi.org/10.1016/j.jmmm.2024.172176

36. Mohamed WS, Tozri A, Abdelbaky MS, García-Granda S, Almutairi TS, Alzaid M, Abu-Dief AM (2024) Effect of heavy Dy^{3+} doping on the magnetic, structural, morphological, and optical characteristics of $CuDy_xFe_{2-x}O_4$ nanoparticles. Ceram Int 50(16):28505–28521. https://doi.org/10.1016/j.ceramint.2024.05.160

37. Ahmad Y, Raina B, Thakur S, Bamzai KK (2022) Magnesium and yttrium doped superparamagnetic manganese ferrite nanoparticles for magnetic and microwave applications. J Magn Magn Mater 552:169178. https://doi.org/10.1016/j.jmmm.2022.169178

38. Almessiere MA, Güner S, Slimani Y, Baykal A, Shirsath SE, Korkmaz AD, et al (2022) Investigation on the structural, optical, and magnetic features of Dy^{3+} and Y^{3+} co-doped $Mn_{0.5}Zn_{0.5}Fe_2O_4$ spinel ferrite nanoparticles. J Mol Struct 1248:131412. https://doi.org/10.1016/j.molstruc.2021.131412

39. Sharma R, Kumar V, Bansal S, Singhal S (2017) Boosting the catalytic performance of pristine $CoFe_2O_4$ with yttrium (Y^{3+}) inclusion in the spinel structure. Mater Res Bull 90:94–103. https://doi.org/10.1016/j.materresbull.2017.01.049

40. Alves TEP, Pessoni HVS, Franco A Jr (2017) The effect of Y^{3+} substitution on the structural, optical band-gap, and magnetic properties of cobalt ferrite nanoparticles. Phys Chem Chem Phys 19:16395. https://doi.org/10.1039/C7CP02167D

41. Chakrabarty S, Dutta A, Pal M (2018) Effect of yttrium doping on structure, magnetic and electrical properties of nanocrystalline cobalt ferrite. J Magn Magn Mater 461:69–75

42. Chakrabarty S, Pal M, Dutta A (2018) Yttrium doped cobalt ferrite nanoparticles: study of dielectric relaxation and charge carrier dynamics. Ceram Int 44(12):14652–14659. https://doi.org/10.1016/j.ceramint.2018.05.091

43. Monisha PGSS, Gomathi SS (2024) Tailoring structural, optical, and magnetic properties of Y^{3+} doped $CoFe_2O_4$ nanoparticles to enhance photocatalytic activity. Ceram Int 50(7):10079–10097. https://doi.org/10.1016/j.ceramint.2023.12.318

44. Rahardjo DT, Budiawanti S, Suharno S, Suryana R, Supriyanto A, Purnama B (2024) Decreasing of magnetic saturation of yttrium doped cobalt ferrite prepared by the sol-gel auto-combustion. Trends Sci 21(4):7320. https://doi.org/10.48048/tis.2024.7320

45. Amin N, Hasan MSU, Majeed Z, Latif Z, un Nabi MA, Mahmood K, et al (2020) Structural, electrical, optical and dielectric properties of yttrium substituted cadmium ferrites prepared by co-precipitation method. Ceram Int 46:20798–20809. https://doi.org/10.1016/j.ceramint.2020.05.079

46. Šiljegović M, Cvejić Ž, Jankov S, Toth E, Herceg D, Odry P, Tadić V (2024) Impedance and dielectric analysis of nickel ferrites: revealing the role of the constant phase element and yttrium doping. Electronics 13(8):1496. https://doi.org/10.3390/electronics13081496

47. Jankov S, Armaković S, Tóth E, Skuban S, Srdic V, Cvejic Z (2019) Understanding how yttrium doping influences the properties of nickel ferrite—combined experimental and computational study. Ceram Int 45:20290–20296. https://doi.org/10.1016/j.ceramint.2019.06.304

48. Ali MA, Khan MNI, Chowdhury F-U-Z, Hossain MM, Hossain AKMA, Rashid R, Nahar A, Hoque SM, Matin MA, Uddin MM (2019) Yttrium-substituted Mg–Zn ferrites: correlation of physical properties with yttrium content. J Mater Sci: Mater Electron. https://doi.org/10.1007/s10854-019-01689-z

49. Ali MA, Khan MNI, Hossain MM, Chowdhury F-U-Z, Hossain MN, Rashid R, Hakim MA, Hoque SM, Uddin MM (2020) Mechanical behavior, enhanced dc resistivity, energy band gap and high temperature magnetic properties of Y-substituted Mg–Zn ferrites. Mater Res Express 7(3):036101. https://doi.org/10.1088/2053-1591/ab7791

50. Karoblis D, Mažeika K, Raudonis R, Žarkov A, Kareiva A (2022) Sol-gel synthesis and characterization of yttrium-doped $MgFe_2O_4$ spinel. Materials 15(21):7547. https://doi.org/10.3390/ma15217547

51. Ivanets A, Prozorovich V, Sarkisov V, Roshchina M, Grigoraviciute-Puroniene I, Zarkov A, et al (2021) Effect of magnesium ferrite doping with lanthanide ions on dark-, visible- and UV-driven methylene blue degradation on heterogeneous Fenton-like catalysts. Ceram Int 47:29786–29794. https://doi.org/10.1016/j.ceramint.2021.07.150

52. Maddi R, Naini PK, Sripada S (2025) Influence of yttrium doping on structural, optical and magnetic properties of $Ni_{0.5}Co_{0.5}Fe_2O_4$ ferrites. Ceram Int 51(26):50985–50995

53. Wu XH, Li LZ, Wu B, Zhong XX, Wang R, Tu XQ, et al (2021) Structure and enhanced electromagnetic properties of Y^{3+} substituted microwave sintered NiZnCo ferrites. Ceram Int 47(3):3720–3727. https://doi.org/10.1016/j.ceramint.2020.09.229

54. Lisser I, Belaiche M, Elansary M, Mouhib Y, Ahmani Ferdi C, Lemine OM, Minaoui K, Tabyaoui M, Salameh B, Alsmadi A (2023) Characterization of Gd-Sm-Y doped barium hexaferrite synthesized by sol-gel auto-combustion: structural, magnetic and DFT investigation. Chem Phys Lett 832:140882. https://doi.org/10.1016/j.cplett.2023.140882

55. Neeradi S, Kotha LR (2025) Effect of Y and Mn on structural, morphological, optical, magnetic properties, photocatalytic and biological activity of cobalt nano ferrites by citrate gel auto combustion method. Polyhedron 117726. https://doi.org/10.1016/j.poly.2025.117726

56. Khan AA, Khan SN, Mir A (2022) Structural and electromagnetic characterization of yttrium doped copper ferrite. J Magn Magn Mater 559:169510. https://doi.org/10.1016/j.jmmm.2022.169510

57. Patil SH, Sujata, Yalburgi S, Angadi VP, Hiremath VG, Deshpande M, et al (2026) Enhanced electrocatalytic hydrogen evolution performance of $NiFe_{2-(x+y)}Y_xCe_yO_4$ spinels synthesized via solution combustion method. Mater Chem Phys 349:131686. https://doi.org/10.1016/j.matchemphys.2025.131686

58. Feng Y, Li S, Zheng Y, Yi Z, He Y, Xu Y (2017) Preparation and characterization of $MgFe_2O_4$ nanocrystallites via PVA sol-gel route. J Alloys Compd 699:521–525. https://doi.org/10.1016/j.jallcom.2016.12.432

59. Araújo JCR, Araujo-Barbosa S, Souza ALR, Iglesias CAM, Xavier J, Souza PB, et al (2021) Tuning structural, magnetic, electrical, and dielectric properties of $MgFe_2O_4$ synthesized by sol-gel followed by heat treatment. J Phys Chem Solids 154:110051. https://doi.org/10.1016/j.jpcs.2021.110051

60. Mohammad AA, Ibrahim NB (2025) Comprehensive study of Ni-substitution yttrium iron garnet: impact of substitution levels and annealing temperature on structural and magnetic properties. J Magn Magn Mater 628:173160. https://doi.org/10.1016/j.jmmm.2025.173160

61. Lahouli R, Massoudi J, Smari M, Rahmouni H, Khirouni K, Dhahri E, Bessais L (2019) Investigation of annealing effects on the physical properties of $Ni_{0.6}Zn_{0.4}Fe_{1.5}Al_{0.5}O_4$ ferrite. RSC Adv 9:19949–19964. https://doi.org/10.1039/C9RA02238D

62. Özçelik B, Özçelik S, Amaveda H, Santos H, Borrell C, Sáez-Puche R, et al (2020) High speed processing of $NiFe_2O_4$ spinel using a laser furnace. J Materiomics 6:661–670. https://doi.org/10.1016/j.jmat.2020.05.003

63. Ajeesha T, Ashwini A, George M, Manikandan A, Mary JA, Slimani Y, et al (2021) Nickel substituted $MgFe_2O_4$ nanoparticles via co-precipitation method for photocatalytic applications. Phys B Condens Matter 606:412660. https://doi.org/10.1016/j.physb.2020.412660

64. Murillo, J.P.M., Abdolrahimi, M., Yaacoub, N. et al. Phase-selective sol–gel auto-combustion synthesis of γ-Fe_2O_3 and Fe_3O_4 nanoparticles. MRS Bulletin 51, 351–363 (2026). https://doi.org/10.1557/s43577-025-01045-z

65. Teber A, Sarac MF (2023) Yttrium-substituted $Co_{0.5}Ni_{0.5}Y_xFe_{2-x}O_4$ ferrites as microwave absorbers by investigating structural, magnetic, dielectric, and absorption characteristics. J Magn Magn Mater 572:170646. https://doi.org/10.1016/j.jmmm.2023.170646

66. Ramzan R, Tariq M, Ashiq MN, Albalawi H, Ahmad I, Alhossainy MH, et al (2021) Effect of yttrium ion on electrical and magnetic properties of barium based spinel ferrites. J Mater Res Technol 12:1104–1112. https://doi.org/10.1016/j.jmrt.2021.03.001

67. Gao S, Wang Z, Chen Y, Wang Y, Fu Q, Feng C (2025) Enhanced gas sensor performances of Y-doped nickel ferrite nanofibers with a rapid response. Ceram Int 51(16):22018–22028. https://doi.org/10.1016/j.ceramint.2025.02.365

68. Luo Q, Wan Y, Wang Z, Gao S, Chen Y, Feng C (2025) Excellent-performing gas sensor based on yttrium-doped $ZnFe_2O_4$ nanofibers for detection of n-butanol. J Alloys Compd [volume and article number to be completed]

69. Umair A, Baig MM, Yousaf S, Touqeer M, Hassan M, Ahmad A, et al (2025) Multiferroic YSn co-doped $BiFeO_3$ 2D nanoplates for enhanced photocatalytic degradation of cationic dyes: synthesis, chemistry and mechanisms. J Water Process Eng 70:107019. https://doi.org/10.1016/j.jwpe.2025.107019

70. Shan A, Baig MM, Kamran U, Jamal H, Arif MU, Hassan M, et al (2024) New $Y_{0.045}Ni_{0.045}Fe_{2.91}O_4$ nanowires decorated over mesoporous silica for crystal violet removal: response surface

methodology optimization, kinetics, and isothermal studies. Ceram Int 50(12):20828–20842. https://doi.org/10.1016/j.ceramint.2024.02.177

71. Hu Y, Liu X, Feng S (2025) Mechanisms influencing ferromagnetic resonance linewidth in Ca–In–Sn co-substituted yttrium–iron garnet ferrites. Materials 18(23):5331. https://doi.org/10.3390/ma18235331

72. Abdo MA, Mansour SF, Al-Bassami NS, Abu-Elsaad NI (2022) Yttrium substituted Co–Cu–Zn nanoferrite: a synergetic impact of Y^{3+} on enhanced physical properties and photocatalysis. Ceram Int 48(11):15314–15326. https://doi.org/10.1016/j.ceramint.2022.02.065

73. Al-Bassami N, Mansour S, Yusuf MBM, Usha N, Alsmail NH, Abdo M (2026) Yttrium-induced modification of structural, magnetic, optical, and photocatalytic characteristics in Ni-Zn–Mn nanoferrites for versatile applications. Ceram Int [volume, pages and DOI to be completed from the publisher record, ScienceDirect PII S0272884225065095]

74. Devkar JV, Patankar KK, Ghone DM, Mathe VL (2021) Investigations of yttrium-doped cobalt–zinc ferrite as potential material for transducer application. Emergent Mater 4(6):1725–1733. https://doi.org/10.1007/s42247-021-00209-2

75. Hemanta Singh H, Basantakumar Sharma H (2020) Investigation on electrical, magnetic and magneto-dielectric properties of yttrium and cobalt co-doped bismuth ferrite nanoparticles. Indian J Phys 94(10):1561–1572. https://doi.org/10.1007/s12648-019-01611-7

76. Datt G, Abhyankar AC (2017) Dopant driven tunability of dielectric relaxation in $M_xCo_{(1-x)}Fe_2O_4$ (M: Zn^{2+}, Mn^{2+}, Ni^{2+}) nano-ferrites. J Appl Phys 122. https://doi.org/10.1063/1.4990275

77. Paswan SK, Pradhan LK, Kumar P, Kumari S, Kar M, Kumar L (2022) Electrical transport properties of nanocrystalline and bulk nickel ferrite using complex impedance spectroscopy: a comparative study. Phys Scr 97:095812. https://doi.org/10.1088/1402-4896/ac87dc

78. Rayssi C, ElKossi S, Dhahri J, Khirouni K (2018) Frequency and temperature-dependence of dielectric permittivity and electric modulus studies of the solid solution $Ca_{0.85}Er_{0.1}Ti_{1-x}Co_{4x/3}O_3$ ($0 \le x \le 0.1$). RSC Adv 8:17139–17150. https://doi.org/10.1039/C8RA00794B

79. Zubkov SV, Parinov IA, Kuprina YA (2022) The structural and dielectric properties of $Bi_{3-x}Nd_xTi_{1.5}W_{0.5}O_9$ (x = 0.25, 0.5, 0.75, 1.0). Electronics 11:277. https://doi.org/10.3390/electronics11020277

80. Arora M, Arora V, Kaur S, Kaur J, Kumar S, Singh A (2023) Evidence of non-Debye behavior of $Pb_{0.76}Sm_{0.24}Ti_{0.76}Fe_{0.24}O_3$ ceramics by complex impedance spectroscopy. Mater Today Proc 80:1079–1085. https://doi.org/10.1016/j.matpr.2022.11.466

81. Karmakar S, Varma S, Behera D (2018) Investigation of structural and electrical transport properties of nano-flower shaped $NiCo_2O_4$ supercapacitor electrode materials. J Alloys Compd 757:49–59. https://doi.org/10.1016/j.jallcom.2018.05.056

82. Guo Y, Huang J, Chen X, Liu Z, Wu J, Gan L, et al (2025) Multifunctional Y-containing $CoFe_2O_4$ for enhanced performance in two-step thermochemical CO_2 splitting. J Environ Chem Eng 118113. https://doi.org/10.1016/j.jece.2025.118113

83. Irfan S, Rizwan S, Shen Y, Li L, Asfandiyar, Butt S, Nan C-W (2017) The gadolinium (Gd^{3+}) and tin (Sn^{4+}) co-doped $BiFeO_3$ nanoparticles as new solar light active photocatalyst. Sci Rep 7:42493 [author list to be confirmed]

84. Bayon A, de la Calle A, Ghose KK, Page A, McNaughton R (2020) Experimental, computational and thermodynamic studies in perovskites metal oxides for thermochemical fuel production: a review. Int J Hydrogen Energy 45:12653–12679. https://doi.org/10.1016/j.ijhydene.2020.02.126

85. Bayon A, de la Calle A, Stechel EB, Muhich C (2022) Operational limits of redox metal oxides performing thermochemical water splitting. Energy Technol 10:2100222. https://doi.org/10.1002/ente.202100222

86. Lu Y, Zhu L, Agrafiotis C, Vieten J, Roeb M, Sattler C (2019) Solar fuels production: two-step thermochemical cycles with cerium-based oxides. Prog Energy Combust Sci 75:100785. https://doi.org/10.1016/j.pecs.2019.100785

87. Randhir K, Rhodes NR, Li L, AuYeung N, Hahn DW, Mei R, et al (2018) Magnesioferrites for solar thermochemical fuel production. Sol Energy 163:1–15. https://doi.org/10.1016/j.solener.2017.12.006

88. Sawaguri H, Gokon N, Hayashi K, Iwamura Y, Yasuhara D (2022) Two-step thermochemical CO_2 splitting using partially-substituted perovskite oxides of $La_{0.7}Sr_{0.3}Mn_{0.9}X_{0.1}O_3$ for solar fuel production. Front Energy Res 10:872959. https://doi.org/10.3389/fenrg.2022.872959

89. Dey S, Naidu BS, Rao CNR (2015) $Ln_{0.5}A_{0.5}MnO_3$ (Ln = lanthanide, A = Ca, Sr) perovskites exhibiting remarkable performance in the thermochemical generation of CO and H_2 from CO_2 and H_2O. Chem Eur J 21:7077–7081. https://doi.org/10.1002/chem.201500442

90. Takalkar G, Bhosale R, AlMomani F (2019) Combustion synthesized $A_{0.5}Sr_{0.5}MnO_{3-\delta}$ perovskites (A = La, Nd, Sm, Gd, Tb, Pr, Dy, and Y) as redox materials for thermochemical splitting of CO_2. Appl Surf Sci 489:80–91. https://doi.org/10.1016/j.apsusc.2019.05.284

91. Nair MM, Abanades S (2018) Experimental screening of perovskite oxides as efficient redox materials for solar thermochemical CO_2 conversion. Sustain Energy Fuels 2:843–854. https://doi.org/10.1039/c7se00516d

92. Takalkar G, Bhosale RR, AlMomani F, Rashid S, Qiblawey H, Saleh Saad MA, et al (2021) Thermochemical splitting of CO_2 using solution combustion synthesized lanthanum-strontium-manganese perovskites. Fuel 285:119154. https://doi.org/10.1016/j.fuel.2020.119154

93. Luciani G, Landi G, Aronne A, Di Benedetto A (2018) Partial substitution of B cation in $La_{0.6}Sr_{0.4}MnO_3$ perovskites: a promising strategy to improve the redox properties useful for solar thermochemical water and carbon dioxide splitting. Sol Energy 171:1–7. https://doi.org/10.1016/j.solener.2018.06.058

94. Jouannaux J, Haeussler A, Drobek M, Ayral A, Abanades S, Julbe A (2019) Lanthanum manganite perovskite ceramic powders for CO_2 splitting: influence of Pechini synthesis parameters on sinterability and reactivity. Ceram Int 45:15636–15648. https://doi.org/10.1016/j.ceramint.2019.05.075

95. Liu X, Wang T, Gao K, Meng X, Song C, Zhu Z, et al (2021) Ca- and Ga-doped $LaMnO_3$ for solar thermochemical CO_2 splitting with high fuel yield and cycle stability. ACS Appl Energy Mater 4:9000–9012. https://doi.org/10.1021/acsaem.1c01274

96. Wang L, Ma T, Dai S, Ren T, Chang Z, Dou L, et al (2020) Experimental study on the high performance of Zr doped $LaCoO_3$ for solar thermochemical CO production. Chem Eng J 389:124426. https://doi.org/10.1016/j.cej.2020.124426

97. Bhosale RR, Takalkar GD (2018) Nanostructured co-precipitated $Ce_{0.9}Ln_{0.1}O_2$ (Ln = La, Pr, Sm, Nd, Gd, Tb, Dy, or Er) for thermochemical conversion of CO_2. Ceram Int 44:16688–16697. https://doi.org/10.1016/j.ceramint.2018.06.096

98. Bulfin B, Miranda M, Steinfeld A (2021) Performance indicators for benchmarking solar thermochemical fuel processes and reactors. Front Energy Res 9:677980. https://doi.org/10.3389/fenrg.2021.677980

99. Dastjerdi OD, Shokrollahi H, Raad NA (2021) Magnetic behavior and characterization of La, Pr, and Bi substituted yttrium iron garnet. Mater Chem Phys 259:124067. https://doi.org/10.1016/j.matchemphys.2020.124067

100. Yang Y, Yu Z, Guo Q, Sun K, Guo R, Jiang X, et al (2018) Thermomagnetization characteristics and ferromagnetic resonance line width broadening mechanism for Ca-Sn co-substituted YIG ferrites. Ceram Int 44:11718–11723. https://doi.org/10.1016/j.ceramint.2018.03.249

101. Cao H, Zheng H, Fan L, Cheng Z, Zhou J, Wu Q, et al (2020) Structural, morphological, dielectric and magnetic properties of Zn-Zr co-doping yttrium iron garnet. Int J Appl Ceram Technol 17:813–822. https://doi.org/10.1111/ijac.13335

102. Gao F, Li J, Su H, Sun Y, Yang Y, Wang G, et al (2021) Low dielectric loss and narrow FMR linewidth of Ca-Ge co-substituted YInIG ferrites for microwave device application. J Alloys Compd 885:160965. https://doi.org/10.1016/j.jallcom.2021.160965

103. Karoblis D, Zarkov A, Garskaite E, Mazeika K, Baltrunas D, Niaura G, et al (2021) Study of gadolinium substitution effects in hexagonal yttrium manganite $YMnO_3$. Sci Rep 11:2875. https://doi.org/10.1038/s41598-021-82621-6

104. Hasan MS, Ali SS, Khan MI, Rizwan M, Zulqarnain M, Hussain A (2023) Structural, optical, electrical and magnetic tuning based on Zn substitution at A site in yttrium doped spinel ferrites. Mater Chem Phys 301:127538. https://doi.org/10.1016/j.matchemphys.2023.127538